Contemporary Mathematics
http://ojs.wiserpub.com/index.php/CM/

UNIVERSAL WISER PUBLISHER

Research Article

Enhanced Energy Transfer Performance in an Inclined Magneto-Convective Sutterby Ternary Hybrid Nanoflow: Application for Nano Diesel

R. Revathi, T. Poornima*

Department of Mathematics, School of Advanced Sciences, Vellore Institute of Technology, Vellore-632014, Tamil Nadu, India
E-mail: poornima.t@vit.ac.in

Received: 26 November 2023; **Revised:** 22 January 2024; **Accepted:** 21 March 2024

Abstract: This study investigates sodium alginate-based nano-lubricants with added copper and aluminum oxides. The thermal performance of nano (Al_2O_3), hybrid (Al_2O_3 + CuO) and ternary (Al_2O_3 + CuO + TiO_2) nanofluids is studied and compared in this article. Due to the significant impact of higher stream rates, the ternary nanofluid is crucial in domains such as petroleum engineering. A Sutterby nanoflow model past a stretching sheet embedded in permeable media is considered. In this fluid, the effects of thermal radiation, hotness source/sink, inclined magneto-convection under Stefan blowing, and chemical reaction are assumed. The highest-order nonlinear partial differential equation is handled by utilizing the similarity function, producing a new set of ordinary differential equations. The derived equations are then quantitatively analyzed using the bvp4c approach in MATLAB.Graphical representations of several features for specific non-dimensional variables, including heat transfer, Sherwood, drag coefficient, velocity, temperature, and concentration, are presented. An increase in the thermal curve is observed due to the heat source/sink parameter; however, the Nusselt number exhibits the opposite pattern. The participation of *Nb* and the thermophoresis force led to greater thermal radiation. For *Sc* and *Kr*, the mass transfer ratio of the ternary nanofluid is lower. The results show very good congruence when compared to the literature. Our results also prove that the ternary hybrid nanofluid transfers more heat from the system than the hybrid or nanofluid. With an increase in Stefan blowing, the rate of energy and mass transfer rises, while the local skin friction coefficients show a tendency in the opposite direction.

***Keywords*:** chemical reaction, inclined magnetic field, porous medium**,** sutterby nanoflow model, stefan blowing condition, thermophoretic process, thermalradiation, ternary nanofluid

MSC: 35Q79

Highlights: Suspending all these three tiny particles into sodium alginate-based nanofluid, the thermal transfer is higher in trihybrid nanoflow than the remaining combos. The outcomes describe the ternary hybrid nanofluid thermal profile increased through the escalation in radiation parameters. Presence of Aluminium oxide helps the complete fuel burn and improves engine performance leading to increased brake thermal efficacy and reduced brake specific fuel consumption. Reduces carbon monoxide emissions, unburnt hydrocarbons (HC), and smoke to better extent and acts as a lubricant, potentially reducing wear and tear in engine components.

DOI: https://doi.org/10.37256/cm.5220243998

Nomenclature

Dimensional variables

T^*	Temperature (K)
C^*	Concentration (mol/m^3)
B_0	Magnetic force strength (kgs^{-2}/A^{-1})
T^*_w	Temperature gradient at walls (K)
k	Thermal conductivity (Wbm^{-1})
μ	Dynamic viscosity (kgm^{-1}s^{-1})
v	Kinematic viscosity (m^{2}s^{-1})
ρ	Density of the fluid (kgm^{-3})
σ	Electrical conductivity (Sm^{-1})
D_B	Brownian diffusivity factor (m^{2}s^{-1})
D_T	Thermophoresis diffusivity factor (m^{2}s^{-1})
σ^*	Stefan-Boltzmann constant (WK^{-4}m^{-2})
C_p	Specific heat (JKg^{-1}K^{-1})
Q	Heat source and sink (Wm^{-3}K^{-1})
u^*, v^*	Velocity in x & y direction (ms^{-1})
x, y	Cartesian coordinates (m)
u_∞	Speed of mainstream (ms^{-1})
C^*_∞	Fluid concentration exterior (mol/m^3)
T^*_∞	Exterior temperature (K)
g	Gravity (ms^{-2})
C^*_w	Wall of concentration (mol/m^3)
q_m	Mass flux (kgm^{-2}s^{-1})
U_w	Speed of the wall (ms^{-1})

Dimensionless variables

η	Similarity variable
f, θ, ϕ	Displacement, energy and species concentration
ϕ_1, ϕ_2, ϕ_3	Volume fraction of Al_2O_3, CuO, TiO_2 nanoparticle
λ	Porosity
Sh	Sherwood
Nb	Brownian motion parameter
Nt	Thermophoresis parameter
Nr	Radiative parameter
Re	Reynolds number
Pr	Prandtl number
γ	Biot number
Nu	Nusselt number
Cf	Wall drag coefficient
ϑ	Angle of magnetic field
Sc	Schmidt number
Kr	Chemical reaction
S	Stefan blowing parameter

Abbreviation

SA	Sodium Alginate
flu	Fluid
nanf	Nanofluid
hybnf	Hybrid nanofluid
terhnf	Ternary hybrid nanofluid

1. Introduction

Fluids exhibit distinct behaviors depending on whether they are classified as Newtonian or non-Newtonian. In contrast to Newtonian fluids adhering to Newton's law, non-Newtonian fluids showcase a variable coefficient of viscosity (shear rate to shear stress ratio) determined by the shear rate. These fluids undergo alterations in viscosity or flow characteristics under stress, becoming either more fluid or thickening to solid-like behavior when pressure is applied. Upon relieving the strain, they revert to their initial state. Unlike Newtonian fluids, common substances like paint, shampoo, and blood exhibit non-Newtonian behavior. Biodiesel primarily serves as a transportation fuel for various vehicle engines, often blended in diverse ratios with petroleum-derived diesel. Sustainable biodiesel finds application in fuel filters, oil spill clean-ups, heated oils, and generators designed to operate on biodiesel [1]. Nano-diesel applications are shown in Figure 1.

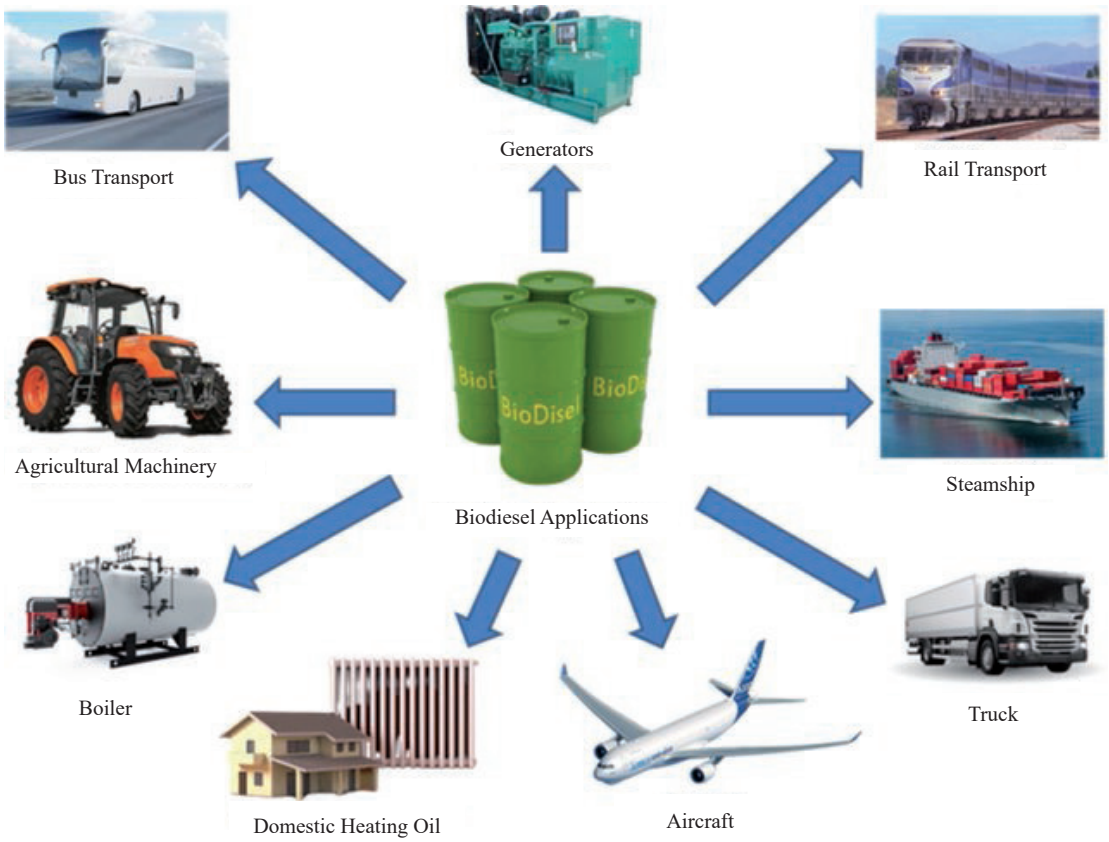

Figure 1. Nano-dieselapplication

Due to the hazardous impact of global warming, there is a necessity of energy transfer or cooling of systems.

Miniaturization needs rapid heat transfer from the system such as micro channels enclosures, and deforming tubes are a few common techniques to improve heat transfer in thermal devices and energy schemes [2-4]. In everyday life, heat transmission occurs almost everywhere, also in the engineering processes like packed-bed storage tanks, grain storage, packed-bed catalytic reactors. These techniques, albeit conventional, are ineffective when dealing with small-scale systems, high heat flux, and quick heat transfer. Enhancing the working fluid's capability for thermophysical and heat transmission will be a suitable solution in this case. Better than conventional working fluids in transferring heat are nanofluids, which have stable dispersions of nanoscale particles in them [5]. Mono and binary nanofluids, which include the dispersion of two distinct types of particles, are the primary topics of research. HNFs are fluids created by dispersing two or more nanoparticles. When compared to NFs across a stretched sheet, these fluids exhibit a larger thermal conductivity. Entropy formation in Carreau ternary hybrid nanofluid flow across a stretched sheet was studied is examined by Nandi and Vajravelu [6], and Mahabaleshwar and Maranna [7] investigated. An investigation into the effect of radiation on the laminar flow of dusty terhnf across porous stretching or shrinking sheets with density transpiration. Ali and Reza-E-Rabbi [8] investigated the combined steady-state effects of thermoelectric and radiation on hydroelectric nanofluid flow across a nonlinear stretching sheet.

In thermal engineering applications, nanofluids stand out as widely used materials, primarily owing to their robust thermal conductivity. This enhanced thermal conductivity has significantly bolstered the efficiency of energy transmission, elevating nanofluids to a prominent position in research endeavors. Hussein [9] delved into the thermal characteristics of laminar nanofluid flow within a tube design. The study revealed an improvement in heat conductivity with increasing nanoparticle fractions. In another investigation, Hussein [10] explored the impact of non-similar modeling on the thermal transport analysis of mixed convective flows of nanofluids over a vertically permeable surface. Gibanov [11] conducted a study on the magnetohydrodynamic (MHD) mixed convection of nanofluid in a cavity with an isothermal local heater, considering the influence of velocity modulation of the upper cold wall. Rehman [12] studied the effect of the Cattaneo-Christov heat flux case on Darcy-Forchheimer flow of Sutterby nanofluid with chemical reactive and thermal radiative impacts. Bouslimi [13] considered the thermal properties, flow, and comparison between Cu and Ag nanoparticles suspended in sodium alginate as Sutterby nanofluids in a solar collector. Sajid [14] scrutinized the impact of gold nanoparticles, along with Maxwell velocity and Smoluchowski temperature slip boundary conditions, on fluid flow: Sutterby model.

Alumina is often used in ventilation tubes & sterilization of equipment and TiO_2 is also used in food additives because it has a dazzling white colour and has unique properties such as being non-noxious, non-sensitive, fluorescent, and photo catalytic. This kind of nanoparticle can fight cancer cells. Xuan et al. [15] investigated the stability and thermo economic potential of a water-based tri-hybrid nanofluid. Manjunatha et al. [16] confirmed that terhnf has a better thermal conductivity than binary and unary nanofluids. To create a unique coolant, they employed a spherical pattern of nanoparticles. Adun et al. [17] investigated the strength, production, and environmentally friendly effects of terhnf. Animasaun et al. [18] recently conducted an abstract investigation on a based -water terhnf with thermophoresis, arbitrary motion, nanoparticle size part. Terhnf are the utmost sophisticated kind of monofluid. Numerous scholars take employed terhnf as hotness exchanger fluids now diverse schemes to develop nanotechnology, as shown in references [19-21].

The effect of a continuous flow Sutterby fluid across an isothermal seeming was explored by Tetsu et al. [22]. By extending Sutterby work on the fluid flow, Akbar and Nadeem [23] were worked on peristaltic models. Later with blood flow biometrics [24]. The findings were then analytically discussed. In order to analyse the pulsatile flow utilising the MHD effects, Abbas et al. [25] looked into the Sutterby liquid model. Based on the regulating parameters, a numerical result is created. Nawaz et al. [26] reflected a hybnf with ethylene glycol as the basis fluid, utilising the Sutterby liquid model. The current model outperforms a conventional liquid in terms of thermal performance. To create the beginning things on the stretching surface, Sajid et al. [27] examined the flow current Sutterby Maxwell fluid perfect. The temperature-dependent characteristic has been considered and mathematically explored. The effect of combination of hard nanoparticles and Sutterby fluid at the section was shown in Waqas et al. [28]. Poornima [29] investigated the effect of thermal radiation on non-Newtonian nanofluid flow along a stretchable surface with Newton boundary condition. Sutter by fluid stands described as a 0-thickness area with a shear level assortment. The Sutterby fluid model is used to highly represent polymer-dilute liquids. Non-Newtonian study arouse curiosity among the investigators to study and analyse their properties. The effects of variable thermal conductivity on the MHD boundary layer slip flow of ethylene-

glycol-based Cu nanofluids past a stretching sheet with convective boundary conditions, as well as the effects of thermal radiation and chemical reactions on the transient MHD natural convection fluid in the presence of Newtonian heating was presented in [30]. Heat and mass transfer in an excited Casson fluid with nonlinear thermal radiation and convection barriers investigated the thermal radiation effects on MHD boundary layer slip flow over a permeable exponential stretching sheet in the presence of joule heating and viscous dissipation was studied [31]. Manjunatha [32] explores the convective heat transfer in a ternary nanofluid moving past a stretched sheet theoretically. Non-linear radiation and Navier-Slip effects on UCM nanofluid flow via a stretched sheet under Lorentzian force was investigated [33]. Thermal case study of tilted magnetic field-actuated transport of radiated blood Ternary Nanofluid [34]. Non-Newtonian fluid under magnetic force also attracted the researchers in this field. Bhargavi and Poornima [35] investigated the magnetic field impact on energy transfer on a viscous fluid. Dey [36] investigated the magnetohydrodynamic boundary layer flow of a conducting fluid via an exponentially extending or contracting sheet with simultaneous temperature and concentration distribution in a porous material. For its various requirements in power plants, turbines, thermal radiation is inevitable in the analysis of transport of energy. In recent research, a wide range of scientists have examined the thermal characteristics of ternary fluid. Palanisamy et al. [37] studied the description and thermophysical properties of tri-hybrid nanoparticle oxide nanostructures, comprising SiO_2, TiO_2, and Al_2O_3, in base fluid water generated in three unique ratios at 0.1 per concentration. Furthermore, numerous researchers have published papers on the usage and presentations of terhnf (Sohail et al. [38]; Ahmed et al. [39]; Sohail et al. [40]; Chu et al. [41]).

No prior research has been published on the utilization of an inclined angle, heat source, heat sink, thermal radiation, chemical reaction, Stefan blowing, or Biot number in the context of ternary heat transfer using Sutterby nanofluid with a sodium alginate base. As a representative of the fundamental computations of high-polymer aqueous solutions, the Sutterby fluid stands out as Newton's most significant non-compliant fluid. The outcomes of the present research hold potential relevance for the polymer manufacturing sector. The focus of the current study primarily revolves around ternary Sutterby nanofluid, addressing the challenge of heat and mass transfer across a stretching sheet while considering the effects of direct heat and an angled magnetic field. This study also explores ternary nanofluids with variable thermal conductivity, porous medium, Stefan blowing, and Schmidt number, incorporating chemical reactions with velocity, temperature, and concentration conditions. Prior to numerical solution by the MATLAB tool bvp4c, the controlled partial differential equation must be transformed into a set of coupled nonlinear ordinary differential equations. The results illustrate an increased thermal profile of the tri-hybrid nanofluid through an escalation in the radiation parameter, while the participation of *Nb* and the thermophoresis force contributes to greater thermal radiation. Additionally, for chemical reaction augment, the mass transfer ratio of the ternary nanofluid is lower.

Assumptions: The following physical criteria connected are to the ternary nanofluid model for stretching sheets:

• In the typical Sutterby fluid, the ternary nanoparticles are homogenously dissolved.

• The ternary nanoparticles and Sutterby fluid, which are the fluid's constituent parts, are undergoing a chemical reaction.

• The energy model also accounts for the impact of thermal convection.

• Over the stretching sheet, Stefan blowing is assumed, and the fluid flow under the convective boundary condition is non-compressible and of a transitory character.

2. Mathematical model

Assume that a laminar flow of an incompressible tri-hybrid nanofluid Al_2O_3, CuO and TiO_2 is created by suspending these particles in *SA*. This may be achieved by considering the hybrid nanofluid Al_2O_3 + CuO/SA and the mono fluid Al_2O_3/SA as the base fluid. At a velocity whose components are (u, v) along (x, y) direction, it is permitted to pass by a stretched sheet. The Cartesian coordinate system describes the physical arrangement, which is seen in Figure 2. In actuality, the magnetic field inclination is the angle formed by the magnetic field lines concerning the horizontal. Indicating that the field is directed into the sheet surface and downward are positive values of inclination. This item has a 45° angle of inclination. This is because the influence of the magnetic field on fluid particles rises with an increase in angle of inclination (ϑ = 0°, 45°, 60°, 90°), which amplifies the Lorentz force and thus diminishes the fluid flow. It is noteworthy that the fluid particles experience maximal resistance when ϑ is greater than 90°. At a speed of $U_w = ax$,

the sheet is supposed to be stretching. The sheet is subjected to a homogeneous magnetic field with a strength of B_0. Moreover, wall temperature and concentration are shown by T_w^* and C_w^*, whereas ambient temperature and concentration are shown by T_∞^* and C_∞^* these presumptions form the basis of the governing equations. The expressions ρ_{terhnf} denotes the density of terhnf, αterhnf denotes thermal diffusivity, Cp stands for the specific heat of the nanofluid, k_{terhnf} for thermal conductivity of the nanofluid, and ϕ for the volume fraction of nanoparticles, in that order.

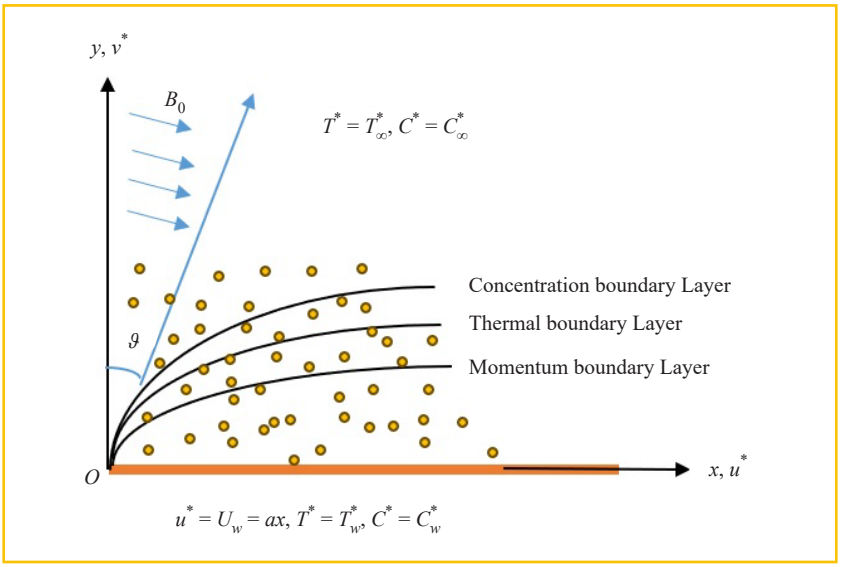

Figure 2. Physical configuration

2.1 *Stress-tensor of Sutterby fluid*

In Sutterby-type fluid, the stress tensor is defined as [42].

$$T = -pI + S,$$

Where S represents the additional stress tensor and p and I represent the pressure and identity tensors, respectively, may be understood as

$$S = -\mu_0 \left[\frac{\sinh^{-1}(E\dot{\gamma})}{E\dot{\gamma}} \right]^m A_1,$$

Where E and μ_0 stand for the material time constant and zero shear rate viscosity, respectively. Below are the mathematical equations for the first-order Rivilian-Erikson tensor A_1 and the second-invariant strain tensor γ, and

$$\dot{\gamma} = \sqrt{\frac{tr(A_1)^2}{2}},$$

and

$$A_1 = (grad\, V) + (grad\, V)^T.$$

The fluid works like Newtonian fluid in the status of $m = 0$, $m > 0$ pseudoplastic (shear thinning), and $m < 0$ dilatant (shear-thickening).

The following are the governing equations (refer to Manjunatha [32] and Li [43]), which are based on the estimations exposed to convective boundary conditions by using the Manjunatha [32] and Konai [44] model for the nanofluid.

$$\frac{\partial u^*}{\partial x} + \frac{\partial v^*}{\partial y} = 0, \tag{1}$$

$$u^* \frac{\partial u^*}{\partial x} + v^* \frac{\partial u^*}{\partial y} = \frac{\mu_{terhnf}}{\rho_{terhnf}} \frac{\partial^2 u^*}{\partial y^2} + \frac{mA^2}{2} \left(\frac{\partial u^*}{\partial y} \right)^2 \left(\frac{\partial^2 u^*}{\partial y^2} \right) - \frac{\sigma_{terhnf}}{\rho_{terhnf}} B_0^2 \sin^2(\vartheta) u^* - \frac{\mu_{terhnf}}{\rho_{terhnf} k^*} u^*, \tag{2}$$

$$u^* \frac{\partial T^*}{\partial x} + v^* \frac{\partial T^*}{\partial y} = k_{terhnf} \frac{\partial^2 T^*}{\partial y^2} + \tau \left[D_B \frac{\partial C^*}{\partial y} \frac{\partial T^*}{\partial y} + \left(\frac{\partial T^*}{\partial y} \right)^2 \left(\frac{D_T}{T_\infty^*} \right) \right] + Q_c (T^* - T_\infty^*) - \frac{1}{(\rho c_p)_{terhnf}} \frac{\partial q_r}{\partial y}, \tag{3}$$

$$u^* \frac{\partial C^*}{\partial x} + v^* \frac{\partial C^*}{\partial y} + K_r (C^* - C_\infty^*) = D_B \frac{\partial^2 C^*}{\partial y^2} + \frac{D_T}{T_\infty^*} \frac{\partial^2 T^*}{\partial y^2}, \tag{4}$$

Subjected to the situations

$$u^* = U_w, v^* = -\frac{D_B}{(1 - C_w)} \frac{\partial C^*}{\partial y}, k_{terhnf} \frac{\partial T^*}{\partial y} = -h_t (T_w^* - T^*), C^* = C_w^* \text{ at } y = 0,$$

$$u^* \to 0, T^* \to T_\infty^*, C^* \to C_\infty^* \text{ as } y \to \infty. \tag{5}$$

2.2 *Rosseland approximation*

Because of the thickness of Sutterby's non-Newtonian nanofluids, radiation only travels a short distance. To account for this occurrence, we apply the Rosseland approximation to equation (3) for radiation [45].

$$q_r = -\frac{4\sigma^*}{3k^*} \frac{\partial \overline{T}^4}{\partial y},$$

The radiation used in this investigation is linear, which results in an approximation of the expression of $\overline{T}^4$. Furthermore, the temperature difference in the flow is modest and, therefore $\overline{T}$ may be written as a linear combination of $\overline{T}^4$ using the Taylor series expansion while ignoring the higher-order components. Thus $\overline{T}^4$ decreases to where,

$$\overline{T}^4 = 4\overline{T}\overline{T}_\infty^3 - 3\overline{T}_\infty^4,$$

$$\frac{\partial q_r}{\partial y} = \frac{16\sigma^* \overline{T}_\infty^3}{3k^* \nu_f (\rho c_p)_f} \frac{\partial^2 \overline{T}}{\partial y^2}. \tag{6}$$

The physical quantities are defined as:

$$Cf = \frac{\mu_{terhnf}}{\mu_{flu}(ax)^2} \left[\left(\frac{\partial u^*}{\partial y} \right) + \frac{mB^2}{3} \left(\frac{\partial u^*}{\partial y} \right)^3 \right]_{y=0},$$

$$Nu = -\left(\frac{x\, k_{terhnf}}{k_{flu}(T_w^* - T_\infty^*)} \right) \left| \frac{\partial T^*}{\partial y} \right|_{y=0}$$

and

$$Sh = -\frac{x\, q_m}{D_B(C_w^* - C_\infty^*)}. \tag{7}$$

2.3 *Rheological and thermophysical characteristics*

The thermophysical possessions of Al_2O_3 + CuO + TiO_2/SA tri hybrid nanofluid are [43].

Table 1. Thermophysical flow properties [43] used in this study

Thermophysical characteristics	Nanoparticles and basefluid
Density	$\rho_{terhnf} = (1-\phi_1)\{(1-\phi_2)[(1-\phi_3)\rho_f + \phi_3\rho_3] + \phi_2\rho_2\} + \phi_1\rho_1$
Viscosity	$\mu_{terhnf} = \frac{\mu_{flu}}{(1-\phi_1)^{2.5}(1-\phi_2)^{2.5}(1-\phi_3)^{2.5}}$
Thermal Conductivity	$\frac{k_{terhnf}}{k_{hybnf}} = \frac{k_1 + 2k_{hybnf} - 2\phi_1(k_{hybnf} - k_1)}{k_1 + 2k_{hybnf} + \phi_1(k_{hybnf} - k_1)}$, where $\frac{k_{hybnf}}{k_{nanf}} = \frac{k_2 + 2k_{nanf} - 2\phi_2(k_{nanf} - k_2)}{k_2 + 2k_{nanf} + \phi_2(k_{nanf} - k_2)}$ and $\frac{k_{nanf}}{k_{flu}} = \frac{k_3 + 2k_{flu} - 2\phi_3(k_{flu} - k_3)}{k_3 + 2k_{flu} + \phi_3(k_{flu} - k_3)}$

Table 1. (cont.)

Thermophysical characteristics	Nanoparticles and basefluid
Electrical Conductivity	$\frac{\sigma_{terhnf}}{\sigma_{hybnf}} = \frac{(1+2\phi_1)\sigma_1 + (1-2\phi_1)\sigma_{hybnf}}{(1-\phi_1)\sigma_1 + (1+\phi_1)\sigma_{hybnf}}$ where $\frac{\sigma_{hybnf}}{\sigma_{nanf}} = \frac{(1+2\phi_2)\sigma_2 + (1-2\phi_2)\sigma_{nanf}}{(1-\phi_2)\sigma_2 + (1+\phi_2)\sigma_{nanf}}$ and $\frac{\sigma_{nanf}}{\sigma_{flu}} = \frac{(1+2\phi_3)\sigma_3 + (1-2\phi_3)\sigma_{flu}}{(1-\phi_3)\sigma_3 + (1+\phi_3)\sigma_{flu}}$
A_2	$(1-\phi_1)^{2.5}(1-\phi_2)^{2.5}(1-\phi_3)^{2.5}$

Table 2. The thermophysical properties encompassing the base fluid and nanoparticles [46-47] used in this study

	SA	Al_2O_3	CuO	TiO_2
ρ (Density, Kgm^{-3})	989	3,970	6,320	4,250
σ (Electrical Conductivity, Sm^{-1})	2.6×10^{-4}	1.00×10^{-10}	2.70×10^{-8}	6.27×10^{-5}
k (Thermal Conductivity, $[W(mk)^{-1}]$)	0.6376	40	76.5	8.9538
C_p (J/kgK)	4,175	765	531.8	686.2

2.4 *Dimensionless form through similarity transformation*

The following similar transformation is used to make the partial differential equations (1) through (4) dimensionless and translate them into ordinary differential equations [32]:

$$u^* = axf'(\eta),\ v^* = -(av)^{1/2} f(\eta),\ \theta(\eta) = \frac{T^* - T_\infty^*}{T_w^* - T_\infty^*},\ \phi(\eta) = \frac{C^* - C_\infty^*}{C_w^* - C_\infty^*},\ \eta = \left(\frac{a}{\nu}\right)^{1/2} y, \tag{8}$$

Equation (1) is fulfilled, and the following equations make up the converted system:

$$\frac{\mu_{terhnf}}{\mu_{flu}} f'''\left(1 + \frac{m}{2}\mathrm{Re}\, Def''^2\right) - \frac{\mu_{terhnf}}{\mu_{flu}}\lambda f' + \frac{\rho_{terhnf}}{\rho_{flu}}\left(ff'' - f'^2\right) - \frac{\sigma_{terhnf}}{\sigma_{flu}}(M\sin^2\vartheta) f' = 0, \tag{9}$$

$$\left(\frac{k_{terhnf}}{k_{flu}} + \frac{4}{3}Nr\right)\theta'' + Nb\theta'\phi' + Nt(\theta')^2 + \mathrm{Pr}\left(\frac{(\rho c_p)_{terhnf}}{(\rho c_p)_{flu}} f\theta' + Q\theta\right) = 0, \tag{10}$$

$$\phi'' + \frac{Nt}{Nb}\theta'' + Scf\phi' - ScKr\phi = 0, \tag{11}$$

The associated boundary conditions are:

$$f'(0) = 1,\ f(0) = \left(\frac{1}{Sc}\right)S\varphi',\ \ \theta'(0) = -\gamma(1-\theta(0)),\ \ \varphi(0) = 1,$$

$$f'(\infty) \to 0,\ \ \theta(\infty) \to 0,\ \ \varphi(\infty) \to 0. \tag{12}$$

In this case, $S = \frac{C_w - C_\infty}{1 - C_w}$ stands for the "Stefan blowing" parameter, where $S > 0$ signifies blowing and $S < 0$ denotes suction.

The equation (7) have the form using the similarity variables,

$$\left(\mathrm{Re}_x\right)^{1/2} Cf_x = -\frac{1}{A_2}\left(f''(0) + \frac{m}{3}\mathrm{Re}\, De(f''(0))^3\right),\ Nu_x\left(\mathrm{Re}_x\right)^{-1/2} = -\frac{k_{terhnf}}{k_{flu}}\left(1 + \frac{4}{3}Nr\right)\theta'(0),$$

and

$$Sh_x\left(\mathrm{Re}_x\right)^{1/2} = -\phi'(0). \tag{13}$$

The non-dimensional parameters are defined as follows:

$$M = \frac{\sigma_f B_0^2}{a\rho_f},\ \mathrm{Pr} = \frac{\nu_f}{\alpha_f},\ Q = \frac{Q_0}{(\rho C_p)a},\ Nb = \frac{\tau D_B (C_w^* - C_\infty^*)}{\nu_f},$$

$$Nt = \frac{\tau D_T (T_w^* - T_\infty^*)}{\nu_f T_\infty},\ \lambda = \frac{\nu_f}{ak^*},\ Nr = \frac{16\sigma^* T_\infty^3}{3k^* \nu_f (\rho C_p)_f},$$

$$De = \frac{a^2 B^2}{\nu_f},\ Sc = \frac{\nu_f}{D_B},\ Kr = \frac{K_r}{a},\ \mathrm{Re}_x = \frac{U_w x}{\nu_f}. \tag{14}$$

3. Technical analysis

Using the built-in MATLAB function bvp4c, the equations (8)-(10) and (11) were handled numerically. Figure 3 shows the bvp4c technique flow chart design. Behind the bvp4c Matlab built-in methodology is a numerical operation known as a finite difference scheme, which is often a collocation method of order four. The PDEs that were simulated are converted into ODEs, denoting $f = f(1), f' = f(2), f'' = f(3)$, $\theta = f(4)$, $\theta' = f(5)$, $\phi = f(6)$ and $\phi' = f(7)$. Rather than [0, ∞), the domain of numerical integration is [0, ηmax], where max is a positive integer, such as ηmax = 7. Below is a list of the first-order ODEs' non-dimensionalized system:

$$f = f(1),$$

$$f' = f(2),$$

$$f'' = f(3),$$

$$f''' = \left[\frac{\left(\frac{\mu_{terhnf}}{\mu_{flu}} \right) \lambda f(2) - \frac{\rho_{terhnf}}{\rho_{flu}} (f(1)f(3) - f(2)f(2)) + \frac{\sigma_{terhnf}}{\sigma_{flu}} M(\sin^2 \vartheta) f(2)}{\frac{\mu_{terhnf}}{\mu_{flu}} (1 + 0.5m \operatorname{Re} Def(3) f(3))} \right],$$

$$\theta = f(4),$$

$$\theta' = f(5), \tag{15}$$

$$\theta'' = \left[\frac{-Nbf(5)f(7) - Ntf(5)f(5) - \Pr\left(\frac{(\rho c_p)_{terhnf}}{(\rho c_p)_{flu}} f(1)f(5) + Qf(4) \right)}{\left(\frac{k_{terhnf}}{k_{flu}} + \frac{4}{3} Nr \right)} \right],$$

$$\varphi = f(6),$$

$$\varphi' = f(7), \tag{16}$$

$$\phi'' = -\frac{Nt}{Nb} \left[\frac{-Nbf(5)f(7) - Ntf(5)f(5) - \Pr\left(\frac{(\rho c_p)_{terhnf}}{(\rho c_p)_{flu}} f(1)f(5) + Qf(4) \right)}{\left(\frac{k_{terhnf}}{k_{flu}} + \frac{4}{3} Nr \right)} \right] - Scf(1)f(7) + ScKrf(6). \tag{17}$$

$$f_a(2) - 1, f_a(1) - \frac{f_a(7)}{Sc} S, f_a(5) + \gamma(1 - f_a(4)),$$

$$f_a(6) - 1, f_b(2), f_b(4), f_b(6). \tag{18}$$

After converting it to MATLAB code, run the system to obtain the necessary results displayed graphically.

Boundary value problem employing code in the MATLAB application with 4th-order precision. A residual error module in Bvp4c duplicates the error in numerical simulation. The tabular information and visual simulations provided in this study met the bvp4c tolerance requirement (10^{-5}).

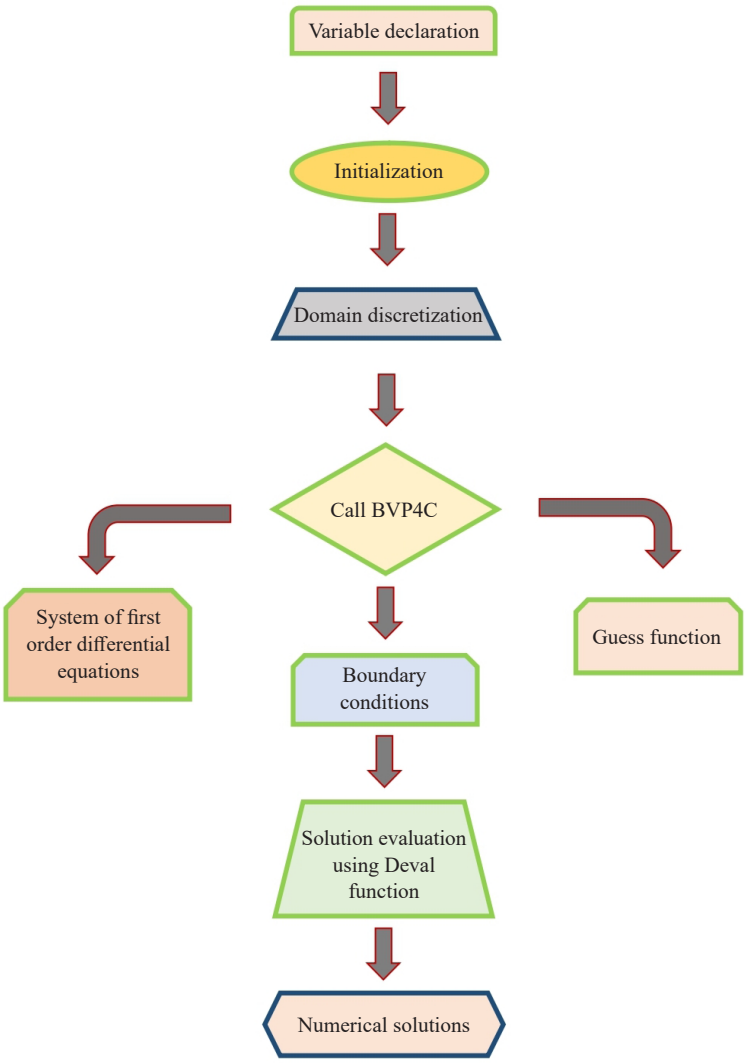

Figure 3. Three stage Lobatto IIIa formula

4. Results and discussion

Boundary value non-linear coupled partial boundary layer equations are solved numerically by the 3-stage Lobatta IIIa formula. Three influential nanoparticles were chosen and whose thermophysical properties are defined in Table 1. Thermophysical properties encompassing the base fluid and nanoparticles in Table 2 and their comparative study is taken over and the upshots are described herewith.

The effects of the magnetic field on the nanoflow velocity profile, temperature profiles are interpreted in Figures 4 and 5, respectively. Figure 4, illustrated that how the velocity vary in the terhnf (Al_2O_3 + CuO + TiO_2/SA), hybnf Al_2O_3 + CuO/SA and nanf Al_2O_3/SA). Compared to the hybnf and nanf, the velocity value is higher for the terhnf when magnetic field parameter value increases. The terhnf describe the same phenomenon that hybnf and nanfs describe, that is the velocity decreases when magnetic field parameter value increases. Also, these fluids obey the following relation terhnf > hybnf > nanf for the velocity. Here the word 'mono' in the figures represent nanofluid with one nanoparticle.

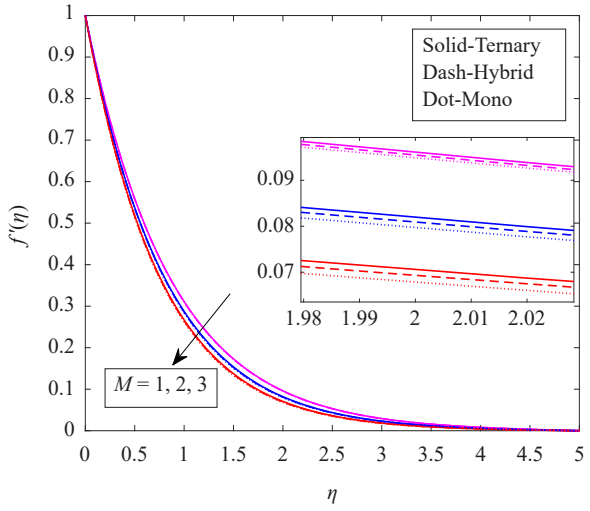

Figure 4. Sway of M on velocity

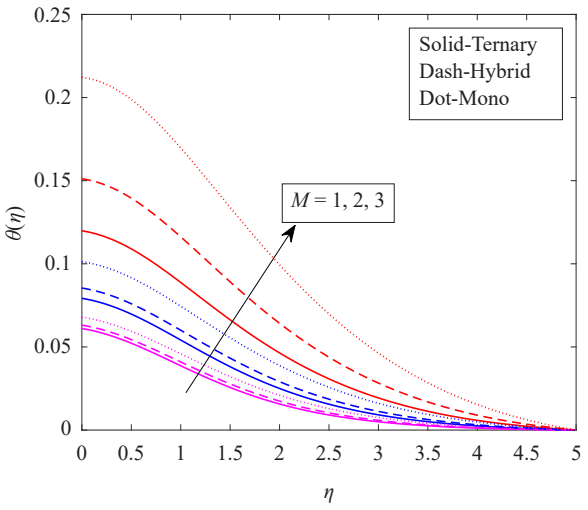

Figure 5. Sway of M on temperature

Table 3. Temperature versus Magnetic Parameter for different nanofluids

M	Temperature at $\eta = 0$		
	Terhnf	Hybnf	nanf
1	0.061	0.063	0.067
2	0.079	0.085	0.101
3	0.119	0.151	0.212

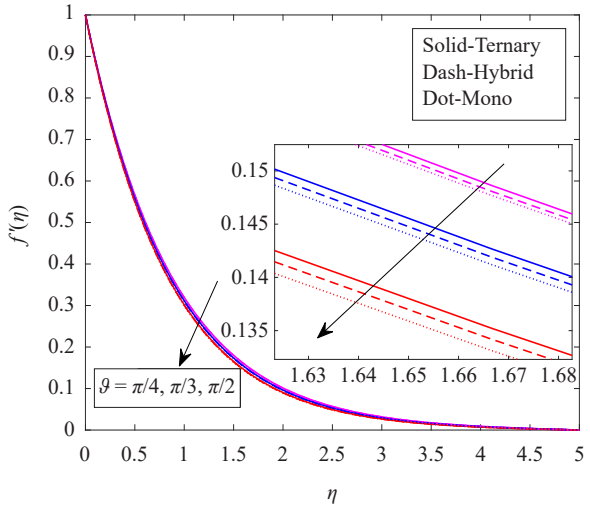

Figure 6. Consequence of ϑ for velocity

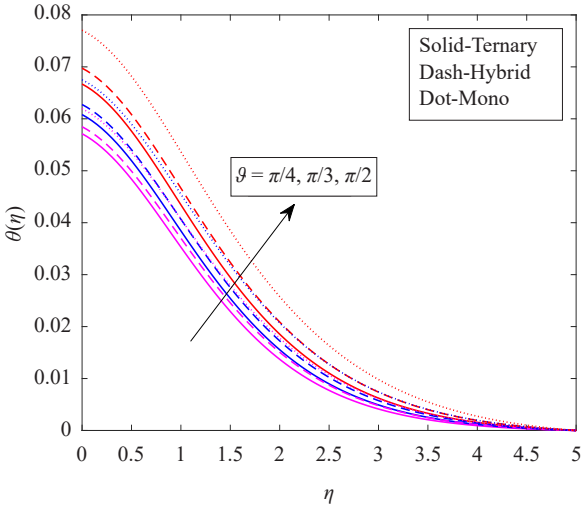

Figure 7. Consequence of ϑ for energy

In Figure 5, we have illustrated the temperature profile by augmenting magnetic field parameter. Compared to the hybnf and nanf, the temperature value is lower for the terhnf when magnetic field parameter value increases. The terhnf describe the same phenomenon that hybnf and nanfs describe, that is the temperature value increases when magnetic field parameter value increases. Also, these fluids obey the following relation terhnf < hybnf < nanf for the temperature value. We have also observed that the temperature slowly increases in the terhnf, ascompared to the hybnf and nanf in Table 3.

Figure 6 displays how the nanoflow velocity modifications for various inclination of magnetic field parameter. Escalating the inclination angle ϑ causes the velocity profiles of nanoflows to fall (Figure 6). The profiles of speed are falling like that of hybrid and nanoflow. Figure 7 displays how the nanoflow energy modifications for various inclination of magnetic field parameter. Escalating the inclination angle ϑ causes the energy profiles of nanoflows to increase (Figure 6). The profiles of momentum are growing as same as that of hybrid and nanoflow.

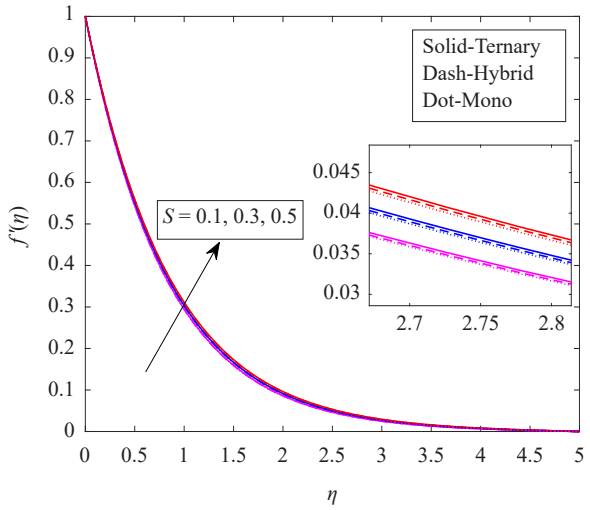

Figure 8. Consequence of S (+values) for Velocity

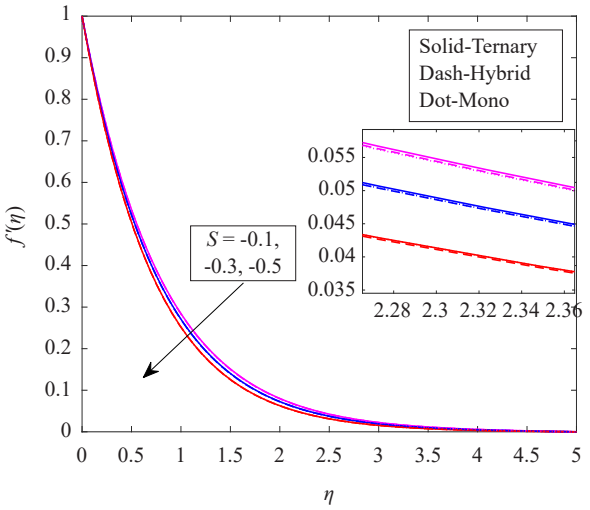

Figure 9. Consequence of S (-values) for Velocity

Figures 8 and 9 displays how the velocity variations for ternary, hybrid, mono (Al_2O_3 + CuO + TiO_2/SA, Al_2O_3 + CuO/SA and Al_2O_3/SA). The velocity goes up as the data for goes up for Stefan blowing, as shown in Figure8. For both hybrid and mono nanofluid. Figure 9 confirmations that for different dropping data for the "Stefan suction" parameter S for steady flows, the liquid's velocity reductions. For mutually hybrid and mono nanf.

Figure 10 displays how the velocity variations for ternary, hybrid, mono (Al_2O_3 + CuO + TiO_2/SA, Al_2O_3 + CuO/SA and Al_2O_3/SA). The outcome of the sponginess λ on speed outlines in stretching sheets. The impact of λ on the velocity profile and temperature. Because the holes in porous media physically enlarge with increasing λ, in this case the drag force acting against the flow direction results in a decrease in the thickness of the velocity boundary layer and a retardation of the velocity. A bigger thermal boundary layer and a greater influence of λ are observed in stable flow as opposed to unstable flow. As the number of pores improves, the flow motion downfalls over the stretching sheet, this is due to the physical phenomena that porosity increase will become obstacle for the fluid to flow.

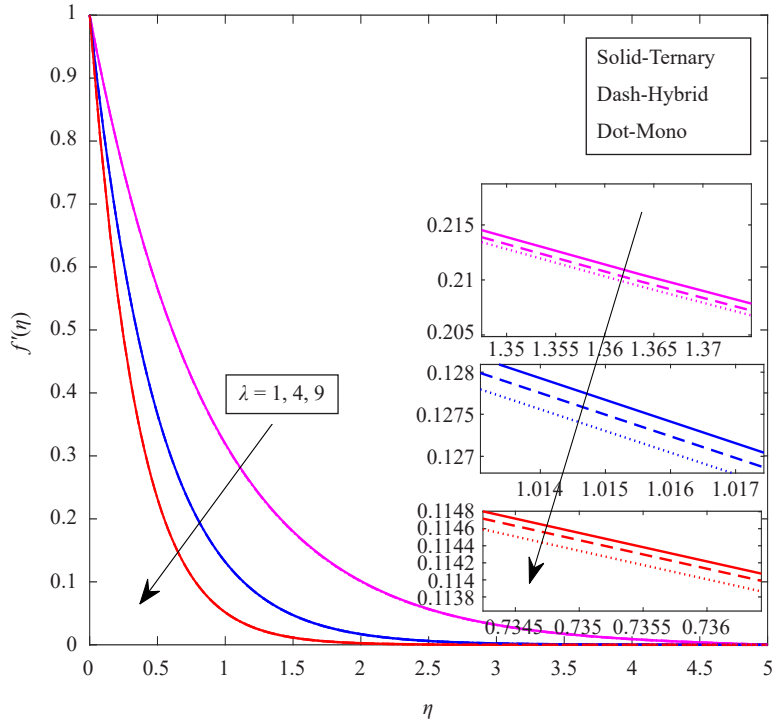

Figure 10. Consequence of λ for Velocity

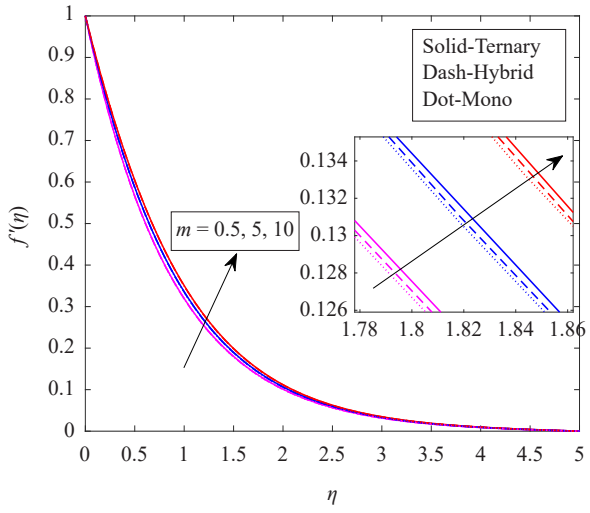

Figure 11. Consequence of *m* for Velocity

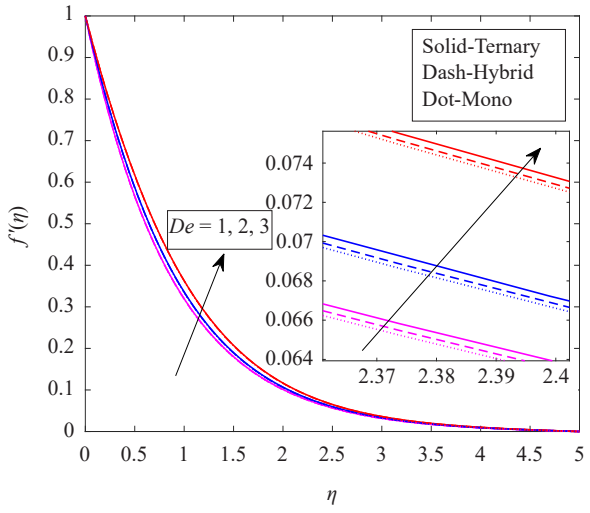

Figure 12. Consequence of *De* for Velocity

Figures 11 and 12 displays how the velocity variations for ternary, hybrid, mono (Al_2O_3 + CuO + TiO_2/SA, Al_2O_3 + CuO/SA and Al_2O_3/SA). Figure 11 shows that the velocity curve rises as the *m* rises. In terms of physics, the parameter *m* determines the fluid's viscosity when shear stress is applied. The fluid properties are often represented as *m*, where $m < 0$, $m > 0$, and Newtonian $m = 0$. Notably, a positive change in *m* causes the fluid flow across a stretched sheet to become less velocity and more viscous (shear thickening). The physical behaviour of shear thickening is attributed to an

increase in the volume fraction of nanoparticles (φ), which increases the fluid viscosity and decreases the fluid velocity $f'(\eta)$. Figure 12 shows that the velocity curve rises as the *De* rises. According to physical principles, the fluid velocity increases and an acceleration is created in the nanofluid flow. In addition, increasing *De* values cause the fluid particles to become more elastic, which reduces friction between them and raises velocity curves as a result.

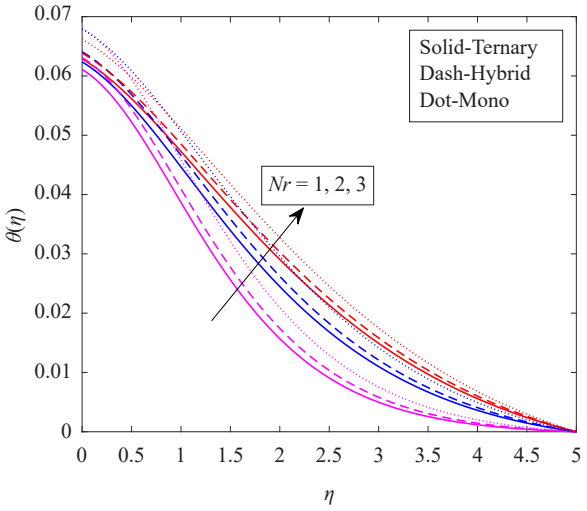

Figure 13. Consequence of *Nr* for Temperature

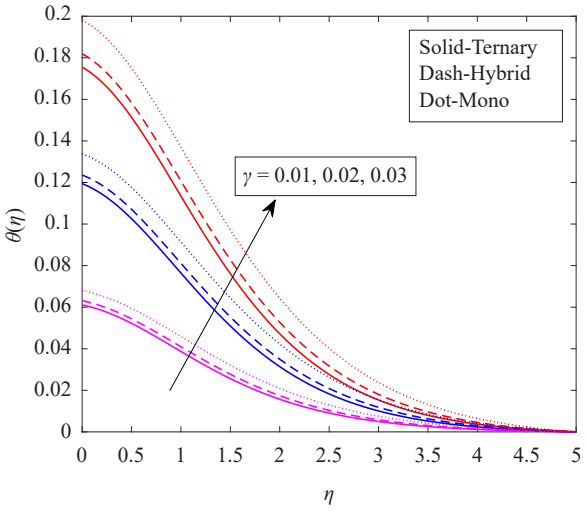

Figure 14. Consequence of γ for Temperature

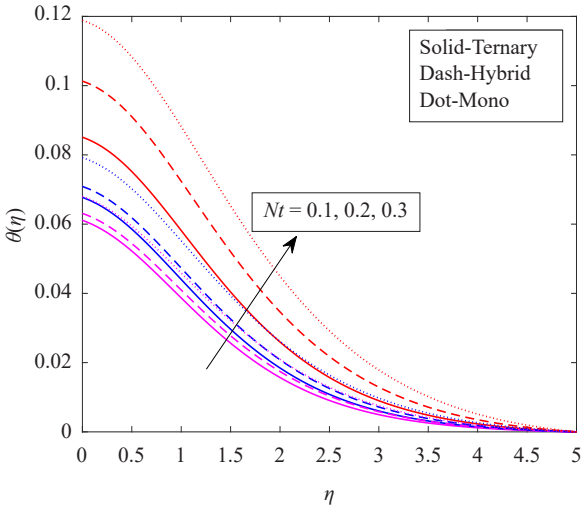

Figure 15. Consequence of *Nt* for Temperature

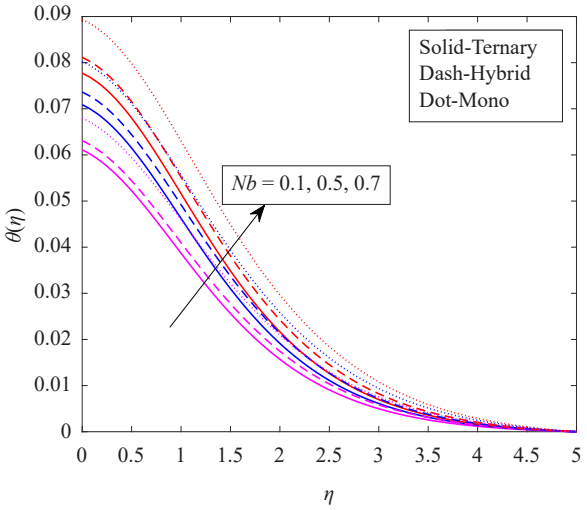

Figure 16. Consequence of *Nb* for Temperature

Figures 13 and 14 shows how the temperature changes for thermal radiation and inclined magnetic strength ternary, hybrid and mono nanf (Al_2O_3 + CuO + TiO_2/SA, Al_2O_3 + CuO/SA and Al_2O_3/SA). The heat profile of nanofluids is presented in figure with the influences of the radiation parameter (*Nr*) shown. In terms of physics, the temperature profiles of the nanofluids rise with an increase in heat generation (*Nr*). The radiative flux drives the nano polymeric wave, which adds thermal energy to the process even when the thermal radiation parameter is raised. The border layer is

nutritious because of its temperature. It has been observed that the enhancing Nr usually intensifies the heat distributions of nanofluids. In view of nanoflows initially decrease and later it starts rising up, moreover it is exhibited that nanoflows shows supremacy than hybrid and trihybrid nanoflows. Figure 14 illustrates the variation in $\theta(\eta)$ with inclination in γ. The thermal profile in this instance is improved by raisin γ. Physically speaking, γ strength provides a thermal boundary layer area augmentation, elevating the $\theta(\eta)$. A thermal field inclination is produced by increasing the γ values, which significantly increases the amount of heat transported by convection.

Figures 15 and 16 shows how the temperature changes for ternary, hybrid and mono nanf (Al_2O_3 + CuO + TiO_2/SA, Al_2O_3 + CuO/SA and Al_2O_3/SA). According to Figure 15, temperature escalations with growing levels of Nt. The purpose of Figure 15 is to examine Nt's impact on $\theta(\eta)$. An increase in Nt raises the fluid temperature. The thermophoresis phenomenon is regarded as the physical cause of such outcomes. Figure 16 exhibits that when hotness upswings, the Brownian motion parameter also upswings. The $\theta(\eta)$ gets better when evaluating Nb on a wider scale. A greater amount of heat transmission is anticipated as a result of the Nb, which is the arbitrary measure of fluid elements. Nanofluid temperature profiles are growing, and the behaviour of the temperature distribution for hybrid and mono nanofluids is comparable. Physically, there are two sources: one is hot and one is cold; particles close to the hot medium absorb heat energy, causing them to move from the hot medium to the cold medium and raise its temperature via convection; this process is known as the thermal potential difference; this is exactly what happens inside the fluid when it is exposed to a heat source. The fluid particles absorb heat energy, which spreads throughout the fluid, raising the temperature and increasing the thickness of the fluid's boundary layer.

5. Validation of results

The perfection of the computational method applied was done by comparing the absolute of heat transfer through the current approach with the verified results of existing literature investigations (Manjunatha and Puneeth [32]; Kon and Pop [48]. The results show their good degree of agreement with the present investigation (Table 4).

Table 4. Comparison values of heat transmission rate $Re^{-0.5}Nu_x$ for various Prandtl numbers, when $m = 0$, $De = 0$, $Re = 0$, $\vartheta = 0$, $\lambda = 0$, $Nt = 0$, $Nb = 0$, $Nr = 0$, $Sc = 0$ and $Kr = 0$

	$Re^{-0.5}Nu_x$		
Pr	Kon and Pop [48]	Manjunatha and Puneeth [32]	Present Study
2	0.9113	0.9113	0.9115
6.13	-	1.7597	1.7598
7	1.8954	1.8954	1.8955

Across the stretching sheet, Figures 17 and 18 shows how the temperature changes for ternary, hybrid and mono nanf (Al_2O_3 + CuO + TiO_2/SA, Al_2O_3 + CuO/SA and Al_2O_3/SA). Figures 17 and 18 visually depict the effects of heat sink ($Q < 0$) and source ($Q > 0$) on the fluid temperature. Figure demonstrates how a heat source ($Q > 0$) raises the temperature. Q's bearing on $\theta(\eta)$ is seen in Figure 17. For higher levels of Q in this case, the heat transmission is enhanced. Increased heat transfer results from the liquid receiving more heat as the heat source process intensity develops.According to physical principles the higher-temperature molecules of the heat source condense their thermal energy to the nearby lower-temperature fluid molecules when they come into contact with the fluid. As a result, the temperature and kinetic energy of the fluid molecules increase. Q's effect on $\theta(\eta)$ is seen in Figure 18. For negative levels of Q in this case, the heat transmission is declined. Decreased heat transfer results from the liquid receiving few energy as the heat sink process intensity drops. But the drop in temperature in mono- and hybrnfs < terhnf. On the

other hand, fluid temperature steadily drops due to the heat sink's influence ($Q < 0$). According to physical principles conduction is the process by which the fluid's higher-temperature molecules transfer their thermal energy to the heat sink's lower-temperature molecules when they come into contact. The fluid molecules lose kinetic energy as a result, and their temperature drops. A heat-absorbing device or medium is called a heat-dissipating media.

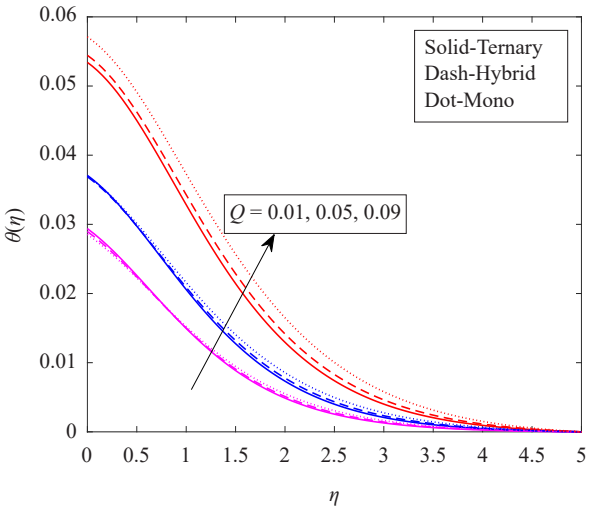

Figure 17. Consequence of Q for Temperature

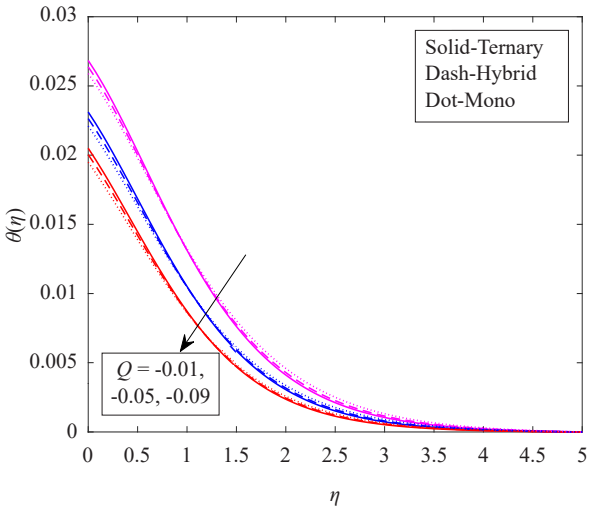

Figure 18. Consequence of Q for Temperature

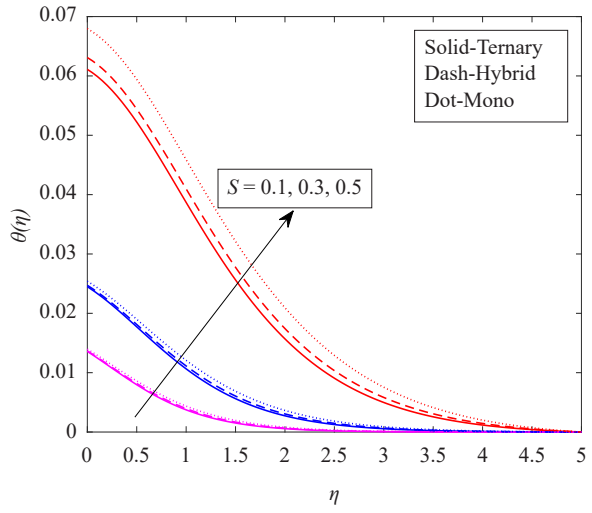

Figure 19. Consequence of S (+) for Temperature

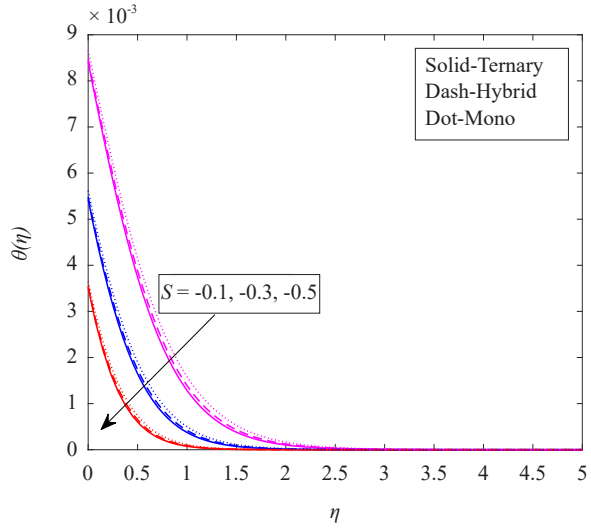

Figure 20. Consequence of S (-) for Temperature

Figures 19 and 20 displays how the temperaturevariations for ternary, hybrid and mono nanf (Al_2O_3 + CuO + TiO_2/SA, Al_2O_3 + CuO/SA and Al_2O_3/SA). The temperature goes up as the data for goes up for Stefan blowing, as shown in Figure 19. For both hybrid and mono nanofluid. Figure 20 confirmations that for different dropping data for the "Stefan suction" parameter S for steady flows, the liquid's temperature reductions. For mutually hybrid and mono nanf.

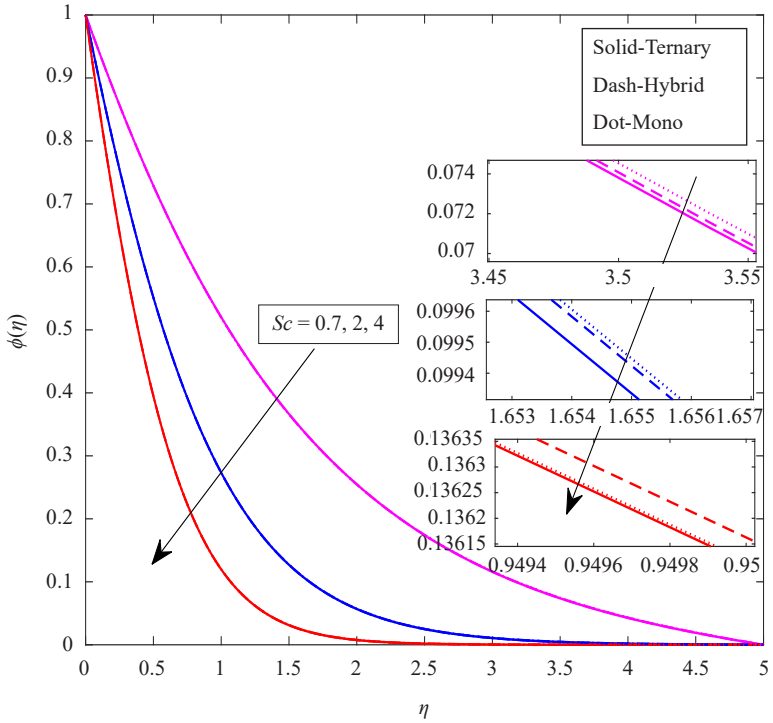

Figure 21. Consequence of *Sc* on Concentration

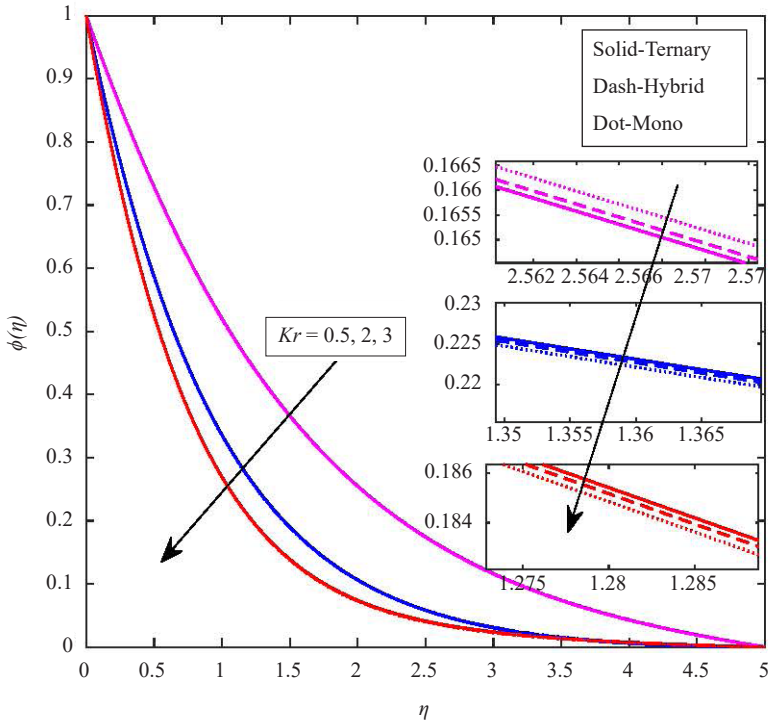

Figure 22. Consequence of *Kr* on Concentration

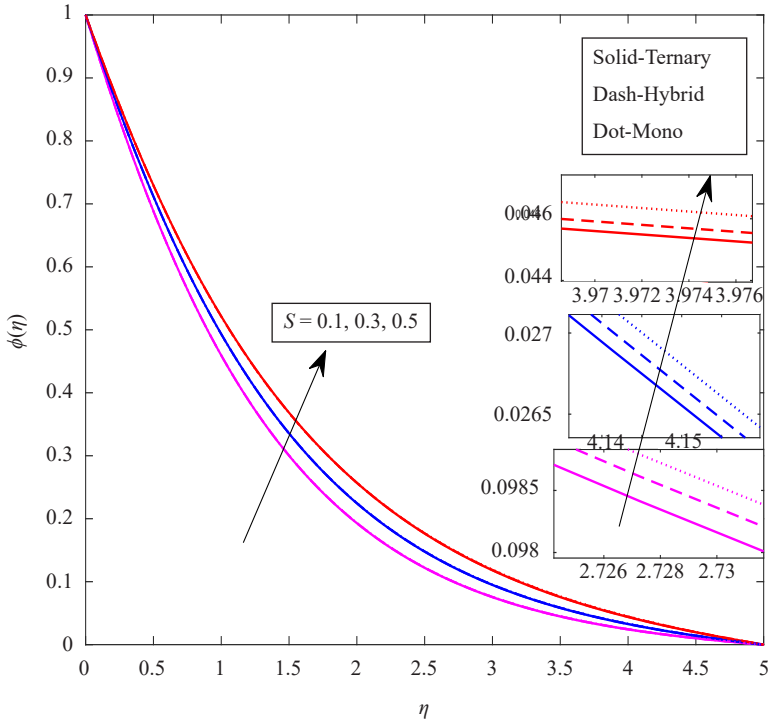

Figure 23. Consequence of S (+) on Concentration

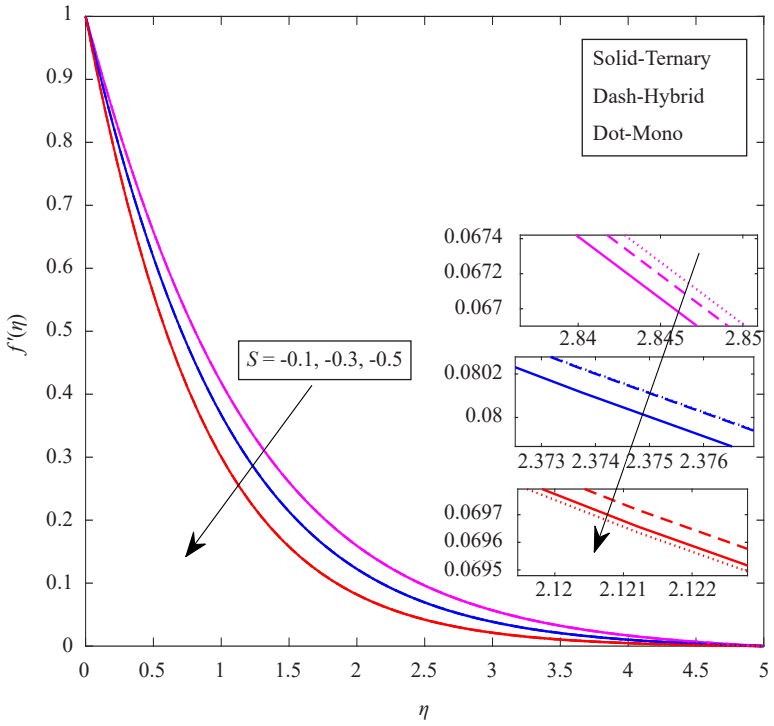

Figure 24. Consequence of S (-) on Concentration

Figures 21 and 22 displays how the Concentration variations for ternary, hybrid and mono nanf (Al_2O_3 + CuO + TiO_2/SA, Al_2O_3 + CuO/SA and Al_2O_3/SA). *Sc* displays the corporal sketch of the mass shape plotted against changed prices of the *Sc*. The growing values of *Sc* enable the identification of the decline in Ternary nanofluid concentration. The fluid's concentration is decreasing because altering *Sc* values makes it possible to reduce molecular diffusivity, which causes the concentration curve to slope downward. Figure 22 highlights the effect of *Kr*. It is obvious from the physical drawing that the fluid concentration falls as *Kr* growths. The mass curve is flattened by the influence of growing values. For both hybrid and mono nanofluid.

Figures 23 and 24 displays how the Concentration variations for ternary, hybrid and mono nanf (Al_2O_3 + CuO + TiO_2/SA, Al_2O_3 + CuO/SA and Al_2O_3/SA). The concentration goes up as the data for goes up for Stefan blowing, as shown in Figure 23. For both hybrid and mono nanofluid. Figure 24 confirmations that for different dropping data for the "Stefan suction" parameter *S* for steady flows, the liquid's Concentration reductions. For mutually hybrid and mono nanf.

The drag coefficient, Sherwood number and Nusselt number trends for ternary Al_2O_3 + CuO + TiO_2/SA and hybrid Al_2O_3 + CuO/SA, mono Al_2O_3/SA nanofluids are illustrated in Tables 5, 6 and 7.

Table 5. Consequences of skin friction for various influencing factors

M	*ϑ*	*m*	*De*	*Re*	*λ*	*γ*	*Nr*	*Nt*	*Nb*	*Q*	*S*	*Sc*	*Kr*	Al_2O_3 + CuO + TiO_2/SA	Al_2O_3 + CuO/SA	Al_2O_3/SA
														-Drag coefficient (*Cf*)		
1	*π*/4	0.5	0.5	0.4	1	0.01	1	0.1	0.1	0.01	0.1	0.7	0.5	1.246224	1.218681	1.191492
2														1.328662	1.302252	1.277179
3														1.405458	1.379564	1.355673
	π/4													1.218816	1.190836	1.162834
	π/3													1.248547	1.221040	1.193918
	π/2													1.278344	1.251277	1.224978
		0.5												1.246224	1.218681	1.191492
		5												1.127636	1.102251	1.077176
		10												1.051093	1.027227	1.003636
			0.5											1.246224	1.218681	1.191492
			5											1.127636	1.102251	1.077176
			15											0.998338	0.975557	0.953026
				0.4										1.246224	1.218681	1.191492
				2										1.183686	1.157246	1.131138
				4										1.127636	1.102251	1.077176
					1									1.246224	1.218681	1.191492
					4									2.128732	2.077816	2.028451
					9									2.990381	2.917441	2.846786
						0.01								1.246224	1.218681	1.191492

Table 5. (cont.)

M	ϑ	m	De	Re	λ	γ	Nr	Nt	Nb	Q	S	Sc	Kr	Al_2O_3 + CuO + TiO_2/SA	Al_2O_3 + CuO/ SA	Al_2O_3/SA
														-Drag coefficient (Cf)		
						0.02								1.245538	1.217976	1.190729
						0.03								1.244835	1.217248	1.189928
							1							1.246224	1.218681	1.191492
							2							1.246406	1.218864	1.191687
							3							1.246497	1.218963	1.191804
								0.1						1.246224	1.218681	1.191492
								0.3						1.244468	1.216844	1.189407
								0.5						1.241062	1.212204	1.183938
									0.1					1.246224	1.218681	1.191492
									0.5					1.246714	1.219185	1.192030
									0.7					1.246744	1.219214	1.192060
										0.01				1.246951	1.219425	1.192281
										0.05				1.246770	1.219247	1.192107
										0.09				1.246396	1.218866	1.191705
										-0.01				1.247012	1.219484	1.192337
										-0.05				1.247104	1.219572	1.192420
										-0.09				1.247170	1.219635	1.192478
											0.1			1.301597	1.272466	1.242724
											0.3			1.271714	1.243453	1.215123
											0.5			1.246224	1.218681	1.191492
											-0.1			1.338976	1.308753	1.277229
											-0.3			1.388972	1.357282	1.323351
											-0.5			1.463143	1.429267	1.391727
												0.7		1.246224	1.218354	1.191492
												2		1.274053	1.244935	1.217299
												4		1.286390	1.256597	1.228600
													0.5	1.246224	1.218681	1.191492
													2	1.196253	1.170131	1.145272
													3	1.172117	1.146750	1.123066

From Table 5 we can easily see that the three influential nanoparticles impacts the friction coefficient.

• Aluminium oxide sodium alginate solution shows its supremacy than other nanfs when friction is considered.

• Al_2O_3 nanf used in water purposes treatment process makes the channels friction free.

• Changing the angle of magnetic force on the nanoflow escalates the skin friction.

• Stefan blowing when acts reduces the drag coefficient whereas suction amplifies it.

• Energy generation diminishes the friction coefficient whilst sinking of energy upsurges the values of Wall shear stress.

• Chemical reaction improves, the friction also condenses.

• Rate of shear stress lessens for Sutterby fluid parameter,in parameters M, ϑ and porosity, respectively, Table 5 demonstrate that when these parameters values rise, the value of skin friction for ternary nanofluid grows more than that of hybrid, mono nanofluid.

• The parameters De, m, and Re. Table 5 shows that when these parameters are reduced, the skin friction values for mono nanofluid decrease more than those for terhnf.

• The relative ternary hotness transfer level% remains constant for the parameters S, Nt, Nb, Sc, Kr, and Q.

Table 6. Results of thermal energy (Nusselt number) for various influencing factors

M	ϑ	m	De	Re	λ	γ	Nr	Nt	Nb	Q	S	Sc	Kr	Al_2O_3 + CuO + TiO_2/SA	Al_2O_3 + CuO/ SA	Al_2O_3/SA
															Nusselt number	
1	π/4	0.5	0.5	0.4	1	0.01	1	0.1	0.1	0.01	0.1	0.7	0.5	0.020937	0.020141	0.019179
2														0.020533	0.019662	0.018493
3														0.019627	0.018248	0.016211
	π/4													0.021026	0.020241	0.019303
	π/3													0.020929	0.020132	0.019167
	π/2													0.020810	0.019995	0.018988
		0.5												0.020937	0.020141	0.019179
		5												0.021119	0.020335	0.019405
		10												0.021226	0.020448	0.019532
			0.5											0.020937	0.020141	0.019179
			5											0.021119	0.020335	0.019405
			15											0.021295	0.020520	0.019611
				0.4										0.020937	0.020141	0.019179
				2										0.021034	0.020246	0.019302
				4										0.021119	0.020335	0.019405
					1									0.020937	0.020141	0.019179
					4									0.022987	0.022133	0.021149
					9									0.022647	0.021829	0.024448
						0.01								0.020937	0.020141	0.020889

Table 6. (cont.)

M	ϑ	m	De	Re	λ	γ	Nr	Nt	Nb	Q	S	Sc	Kr	$Al_2O_3 + CuO + TiO_2/SA$	$Al_2O_3 + CuO/SA$	Al_2O_3/SA
														Nusselt number		
						0.02								0.039271	0.037681	0.035647
						0.03								0.055160	0.052758	0.049501
							1							0.020937	0.020141	0.019179
							2							0.031084	0.030034	0.028770
							3							0.041237	0.039957	0.038431
								0.1						0.020937	0.020141	0.019179
								0.3						0.020789	0.019974	0.018948
								0.5						0.020402	0.019320	0.018132
									0.1					0.020937	0.020141	0.019179
									0.5					0.020719	0.019915	0.018927
									0.7					0.020566	0.019753	0.018739
										0.01				0.021645	0.020875	0.019990
										0.05				0.021473	0.020705	0.019817
										0.09				0.021109	0.020328	0.019403
										-0.01				0.021701	0.020931	0.020045
										-0.05				0.021785	0.021011	0.020123
										-0.09				0.021843	0.021067	0.020177
											0.1			0.021997	0.021204	0.020290
											0.3			0.021754	0.020966	0.020055
											0.5			0.020937	0.020141	0.019179
											-0.1			0.022113	0.021316	0.020399
											-0.3			0.022179	0.021380	0.020462
											-0.9			0.022278	0.021477	0.020557
												0.7		0.020937	0.019958	0.019179
												2		0.021780	0.020834	0.020081
												4		0.021899	0.020952	0.020197
													0.5	0.020937	0.020141	0.019179
													2	0.023830	0.022877	0.021774
													3	0.023710	0.022772	0.021686

From Table 6 we can easily see that Al_2O_3 + CuO + TiO_2/SA, Al_2O_3 + CuO/SA and Al_2O_3/SA when thermal energy (Nusselt number).

• The variables γ and *Nr* correspondingly. Tables 6 show that when the prices of these factors go up, the value of thermal energy for ternary nanofluid grows higher than that of hybnf , mono nanf.

• When the parameters *Nt* and *Nb* are increased, the Nusselt number for ternary, hybrid, and mono nanofluids reduces somewhat.

• 0.01 < *Q* < 0.09 then thermal energy for ternary 0.0216 > 0.0214 > 0.0211, hybrid 0.0208 > 0.0207 > 0.0203 and mono 0.0199 > 0.0198 > 0.0194 tiny falls. Similar Stefan blowing parameter.

• -values in *Q* then thermal energy for ternary, hybrid, and mono nanofluid hardly upsurges. Similar Stefan blowing parameter.

• The relative ternary Nusselt number% remains constant for the parameters *Sc*, *Kr*.

Table 7. Grades of mass diffusion rate (Sherwood number) for several influencing factors

M	ϑ	*m*	*De*	*Re*	λ	γ	*Nr*	*Nt*	*Nb*	*Q*	*S*	*Sc*	*Kr*	Al_2O_3 + CuO + TiO_2/SA	Al_2O_3 + CuO/SA	Al_2O_3/SA
														Sherwood number		
1	π/4	0.5	0.5	0.4	1	0.01	1	0.1	0.1	0.01	0.1	0.7	0.5	0.599597	0.599750	0.600333
2														0.598803	0.599450	0.601505
3														0.601973	0.606391	0.615131
	π/4													0.600234	0.600342	0.600788
	π/3													0.599549	0.599708	0.600307
	π/2													0.599047	0.599307	0.600183
		0.5												0.599597	0.599750	0.600333
		5												0.601451	0.601493	0.601808
		10												0.603245	0.603235	0.603425
			0.5											0.599597	0.599750	0.600333
			5											0.601451	0.601493	0.601808
			15											0.604790	0.604754	0.604884
				0.4										0.599597	0.599750	0.600333
				2										0.600448	0.600537	0.600966
				4										0.601451	0.601493	0.601808
					1									0.599597	0.599750	0.600333
					4									0.555731	0.555933	0.556206
					9									0.541382	0.541355	0.541307
						0.01								0.599597	0.599750	0.600333
						0.02								0.605389	0.605889	0.607315
						0.03								0.611345	0.612237	0.614643

Table 7. (cont.)

M	ϑ	m	De	Re	λ	γ	Nr	Nt	Nb	Q	S	Sc	Kr	$Al_2O_3 + CuO + TiO_2/SA$	$Al_2O_3 + CuO/SA$	Al_2O_3/SA
														Sherwood number		
							1							0.599597	0.599750	0.600333
							2							0.598057	0.598163	0.598545
							3							0.597283	0.597298	0.597480
								0.1						0.599597	0.599750	0.600333
								0.3						0.614444	0.615752	0.619409
								0.5						0.643322	0.656283	0.669576
									0.1					0.599597	0.599750	0.600333
									0.5					0.595448	0.595370	0.595416
									0.7					0.595201	0.595113	0.595136
										0.01				0.593450	0.593282	0.593122
										0.05				0.594983	0.594827	0.594710
										0.09				0.598138	0.598144	0.598386
										-0.01				0.592930	0.592766	0.592606
										-0.05				0.592155	0.592002	0.591851
										-0.09				0.591595	0.591455	0.591317
											0.1			0.705931	0.705951	0.706124
											0.3			0.643705	0.643693	0.643813
											0.5			0.599597	0.599750	0.600333
											-0.1			0.790635	0.790693	0.790167
											-0.3			0.911898	0.912003	0.912434
											-0.5			1.103303	1.103493	1.104216
												0.7		0.599597	0.600022	0.600333
												2		1.048134	1.648090	1.047949
												4		1.520202	1.520126	1.519931
													0.5	0.599597	0.599750	0.600333
													2	1.030656	1.030948	1.031303
													3	1.245472	1.245128	1.244669

From Table 7 we can easily see that $Al_2O_3 + CuO + TiO_2/SA$, $Al_2O_3 + CuO/SA$ and Al_2O_3/SA when mass diffusion rate.

• *Sc* and *Kr* are the related variables. Tables 7 demonstrate that when the values of these parameters increase, the mass diffusion rate of ternary nanofluid increases faster than that of hybrid, mono nanofluid.

• When the values of the Stefan blowing parameters are raised, the mass diffusion rate drops while the negative values for Sherwood grow.

• The relative ternary heat transfer rate% remains constant for the parameters *M*, *Re*, *De*, *m*, γ, ϑ, λ, *Nt*, *Nb*, *Sc*, *Kr*, *S* and *Q*.

6. Conclusion

The ternary (Al_2O_3 + CuO + TiO_2/SA) nanofluid over stretching sheet is examined using the Sutterby fluid theory. The fundamental PDEs are transformed into ODEs by use of similarity transformations. The boundary value problem with 4th order accuracy solver (BVP4C) in the computing programme MATLAB is used to solve the ODEs numerically. By taking the suspension of distinct classes of nanoparticles that fit the realistic scenario into consideration, this work may be further expanded to explore the behaviour of other non-Newtonian fluids under varied physical situations. These are the major ideas of the current work:

• Presence of Aluminium oxide helps the complete fuel burn and improves engine performance leading to increased brake thermal efficacy and reduced brake specific fuel consumption. Reducescarbonmonoxideemissions,unburnt hydrocarbons (HC), and smoke to better extent and acts as a lubricant, potentially reducing wear and tear in engine components.

• Comparisons between pure fluid, nanofluid, and hybrid nanofluid revealed that ternary hybrid nanofluid had superior heat transferors.

• Nonlinear thermal radiations *Nr* are superior for thermal enhancement across a stretching sheet, and ternary nanofluids demonstrated dominating heat transmission.

• When talking about the depth of the limit layer, mass diffusion remains talked about as a function of falling *Sc*, *Kr*, *S*(-values) and rising Stefan blowing (positive values).

• The Sherwood number and the Nusselt number of a ternary hybrid nanofluid go up a little as the power-law index grows. But skin drag goes down as the power law index goes up.

• The effect of porosity, *M* restriction on the speed curve of terhnf is to make it go down.

• When the Stefan blowing values go down, the velocity curve goes down, but when ternary nanoparticles are added to the Stefan blowing values that go up, the velocity of terhnf goes up.

• With the help of heat source Q+ and *Nt*, *Nb*, γ the energy profile rises. The energy profile of a heat sink Q- drops down.

• When the Deborah number and Power-law-index values rise, so does the ternary velocity graph, and ternary nanofluid rises above hybrid and mono nanofluid.

• For determining the best ternary nanofluids for heat-transfer applications in the future, it is advised that the flow issue be addressed with a variety of base liquids, fluid models, and nanoparticles.

• The approach has a drawback in that the disregarded terms at different truncation levels must have an impact on the correctness of the answers.

The current work aims to investigate the dynamic of Sutterby nanofluid stream towards a stretching sheet with Stefan blowing and Biot number condition: Sutterby nanofluid model, as it is considered that this topic has not been thoroughly studied before. In the future, the existing plan may be used to tackle a range of technological and physical problems.

Final thoughts

Ternary nanofluid may be recommended for industrial applications requiring a large level of heat transmission. In thermal transport equipment, such as heat exchangers, radiators, and electronic cooling, nanofluids are generally employed as coolants.

Future scope

The evaluation's conclusions can serve as a guide for future studies that examine the thermal performance of ternary materials using a variety of non-Newtonian nanofluids (think Casson Sutterby, Carreau, Maxwell, micropolar, etc.). Comparable equalities can include multi-dimensional slip Sutterby modalities, temperature-dependent porosity, and viscosity impacts.

Author contributions

R. Revathi formulated and analysed the problem. The manuscript was written collaboratively by the authors. T. Poornima validated the hypothesis, findings, and evaluations and approved the final version.

Acknowledgement

The authors acknowledge the reviewers for their constructive suggestions to improve our work.

Data availability statements

All the data are clearly available in the manuscript.

Conflict of interest

The authors declare no competing financial interest.

References

[1] Nabgan W, Jalil AA, Nabgan B, Jadhav AH, Ikram M, Ul-Hamid A, et al. Sustainable biodiesel generation through catalytic transesterification of waste sources: a literature review and bibliometric survey. *RSC Advances*. 2022; 12(3): 1604-1627.

[2] Husain S, Khan SA. A review on heat transfer enhancement techniques during natural convection in vertical annular geometry. *Cleaner Engineering and Technology*. 2021; 5: 100333.

[3] Roy U, Roy PK. Advances in heat intensification techniques in shell and tube heat exchanger. *Advanced Analytic and Control Techniques for Thermal Systems with Heat Exchangers*. Academic Press; 2020. p.197-207. Available from: doi:10.1016/B978-0-12-819422-5.00007-4

[4] Maradiya C, Vadher J, Agarwal R. The heat transfer enhancement techniques and their thermal performance factor. *Beni-Suef University Journal of Basic and Applied Sciences*. 2018; 7(1): 1-21.

[5] Yasmin H, Giwa SO, Noor S, Sharifpur M. Thermal conductivity enhancement of metal oxide nanofluids: A critical review. *Nanomaterials*. 2023; 13(3): 597.

[6] Nandi S, Vajravelu K. Analysis of entropy generation in Carreau ternary hybrid nanofluid flow over a stretching sheet. *Numerical Heat Transfer, Part A: Applications*. 2023; 1-25. Available from: doi:10.1080/10407782.2023.2233730.

[7] Mahabaleshwar US, Maranna T, Perez LM, Bognár GV, Oztop HF. An impact of radiation on laminar flow of dusty ternary nanofluid over porous stretching/shrinking sheet with mass transpiration. *Results in Engineering*. 2023; 18: 101227. Available from: doi:10.1016/j.rineng.2023.101227.

[8] Ali MY, Reza-E-Rabbi S, Rasel MM, Ahmmed SF. Combined impacts of thermoelectric and radiation on hydromagnetic nanofluid flow over a nonlinear stretching sheet. *Partial Differential Equations in Applied Mathematics*. 2023; 7: 100500.

[9] Hussain M, Khan W, Farooq U, Razzaq R. Impact of non-similar modeling for thermal transport analysis of mixed

convective flows of nanofluids over vertically permeable surface. *Journal of Nanofluids*. 2023; 12(4): 1074-1081. Available from: doi:10.1166/jon.2023.1985
[10] Gibanov NS, Hussain M, Sheremet MA. MHD mixed convection of nanofluid in a cavity with isothermal local heater under an influence of velocity modulation of upper cold wall. *International Journal of Thermal Sciences*. 2023; 192: 108402.
[11] Riaz S, Naheed N, Farooq U, Lu D, Hussain M. Non-similar investigation of magnetized boundary layer flow of nanofluid with the effects of Joule heating, viscous dissipation and heat source/sink. *Journal of Magnetism and Magnetic Materials*. 2023; 574: 170707.
[12] Rehman MI, Chen H, Hamid A, Jamshed W, Eid MR, El Din SM, et al. Effect of Cattaneo-Christov heat flux case on Darcy-Forchheimer flowing of Sutterby nanofluid with chemical reactive and thermal radiative impacts. *Case Studies in Thermal Engineering*. 2023; 42: 102737.
[13] Bouslimi J, Alkathiri AA, Althagafi TM, Jamshed W, Eid MR. Thermal properties, flow and comparison between Cu and Ag nanoparticles suspended in sodium alginate as Sutterby nanofluids in solar collector. *Case Studies in Thermal Engineering*. 2022; 39: 102358.
[14] Sajid T, Jamshed W, Shahzad F, Akgül EK, Nisar KS, Eid MR. Impact of gold nanoparticles along with Maxwell velocity and Smoluchowski temperature slip boundary conditions on fluid flow: Sutterby model. *Chinese Journal of Physics*. 2022; 77: 1387-404.
[15] Xuan Z, Zhai Y, Ma M, Li Y, Wang H. Thermo-economic performance and sensitivity analysis of ternary hybrid nanofluids. *Journal of Molecular Liquids*. 2021; 323: 114889.
[16] Manjunatha S, Puneeth V, Gireesha BJ, Chamkha A. Theoretical study of convective heat transfer in ternary nanofluid flowing past a stretching sheet. *Journal of Applied and Computational Mechanics*. 2022; 8(4): 1279-1286.
[17] Adun H, Kavaz D, Dagbasi M. Review of ternary hybrid nanofluid: Synthesis, stability, thermophysical properties, heat transfer applications, and environmental effects. *Journal of Cleaner Production*. 2021; 328: 129525. Available from: doi:10.1016/j.jclepro.2021.129525.
[18] Animasaun IL, Yook SJ, Muhammad T, Mathew A. Dynamics of ternary-hybrid nanofluid subject to magnetic flux density and heat source or sink on a convectively heated surface. *Surfaces and Interfaces*. 2022; 28: 101654. Available from: doi:10.1016/j.surfin.2021.101654.
[19] Ramadhan AI, Azmi WH, Mamat R, Hamid KA, Norsakinah S. Investigation on stability of tri-hybrid nanofluids in water-ethylene glycol mixture. *IOP Conference Series: Materials Science and Engineering*. 2019; 469(1): 012068. Available from: doi:10.1088/1757-899X/469/1/012068.
[20] Saleem S, Animasaun IL, Yook SJ, Al-Mdallal QM, Shah NA, Faisal M. Insight into the motion of water conveying three kinds of nanoparticles shapes on a horizontal surface: significance of thermo-migration and Brownian motion. *Surfaces and Interfaces*. 2022; 30: 101854.
[21] Cao W, Animasaun IL, Yook SJ, Oladipupo VA, Ji X. Simulation of the dynamics of colloidal mixture of water with various nanoparticles at different levels of partial slip: Ternary-hybrid nanofluid. *International Communications in Heat and Mass Transfer*. 2022; 135: 106069.
[22] Tetsu F, Osamu M, Motoo F, Hiroshi T, Kentaro M. Natural convective heat transfer from a vertical isothermal surface to a non-Newtonian Sutterby fluid. *International Journal of Heat and Mass Transfer*. 1973; 16(12): 2177-2187.
[23] Akbar NS, Nadeem S. Nano Sutterby fluid model for the peristaltic flow in small intestines. *Journal of Computational and Theoretical Nanoscience*. 2013; 10(10): 2491-2499.
[24] Akbar NS. Biomathematical study of Sutterby fluid model for blood flow in stenosed arteries. *International Journal of Biomathematics*. 2015; 8(6): 1550075.
[25] Abbas Z, Shabbir MS, Ali N. Numerical study of magnetohydrodynamic pulsatile flow of Sutterby fluid through an inclined overlapping arterial stenosis in the presence of periodic body acceleration. *Results in Physics*. 2018; 9: 753-762.
[26] Nawaz M. Role of hybrid nanoparticles in thermal performance of Sutterby fluid, the ethylene glycol. *Physica A: Statistical Mechanics and Its Applications*. 2020; 537: 122447.
[27] Sajid T, Tanveer S, Sabir Z, Guirao JL. Impact of activation energy and temperature-dependent heat source/sink on Maxwell-Sutterby fluid. *Mathematical Problems in Engineering*. 2020; 2020: 5251804. Available from: doi:10.1155/2020/5251804.
[28] Waqas H, Farooq U, Bhatti MM, Hussain S. Magnetized bioconvection flow of Sutterby fluid characterized by the suspension of nanoparticles across a wedge with activation energy. *ZAMM-Journal of Applied Mathematics and Mechanics/Zeitschrift für AngewandteMathematik und Mechanik*. 2021; 101(3): e202000349. Available from:

doi:10.1002/zamm.202000349.
[29] Poornima T, Sreenivasulu P, Souayeh B. Thermal radiation influence on non-Newtonian nanofluid flow along a stretchable surface with Newton boundary condition. *International Journal of Ambient Energy*. 2023; 44(1): 2469-2479.
[30] Reddy NB, Poornima T, Sreenivasulu P. Influence of variable thermal conductivity on MHD boundary layer slip flow of ethylene-glycol based Cu nanofluids over a stretching sheet with convective boundary condition. *Int J Eng Math*. 2014; 2014: 905158.
[31] Sreenivasulu P, Poornima T, Bhaskar Reddy N. Thermal radiation effects on MHD boundary layer slip flow past a permeable exponential stretching sheet in the presence of joule heating and viscous dissipation. *Journal of Applied Fluid Mechanics*. 2015; 9(1): 267-278.
[32] Manjunatha S, Puneeth V, Gireesha BJ, Chamkha A. Theoretical study of convective heat transfer in ternary nanofluid flowing past a stretching sheet. *Journal of Applied and Computational Mechanics*. 2022; 8(4): 1279-1286.
[33] Sreenivasulu P, Poornima T, Vasu B, Reddy Gorla RS, Bhaskar Reddy N. Non-linear radiation and Navier-slip effects on UCM nanofluid flow past a stretching sheet under Lorentzian force. *Journal of Applied and Computational Mechanics*. 2021; 7(2): 638-645.
[34] Saleem N, Ashraf T, Daqqa I, Munawar S, Idrees N, Afzal F, et al. Thermal case study of cilia actuated transport of radiated blood-based ternary nanofluid under the action of tilted magnetic field. *Coatings*. 2022; 12(6): 873. Available from: doi:10.3390/coatings12060873.
[35] Bhargavi N, Poornima T, Souayeh B. Magnetohydrodynamic conjugate heat transfer analysis on a viscous fluid past a vertical permeable plate. *International Journal of Modern Physics B*. 2023; 2450211. Available from: doi:10.1142/S0217979224502114.
[36] Dey D, Makinde OD, Borah R. Analysis of dual solutions in MHD fluid flow with heat and mass transfer past an exponentially shrinking/stretching surface in a porous medium. *International Journal of Applied and Computational Mathematics*. 2022; 8(2): 66.
[37] Palanisamy R, Parthipan G, Palani S. Study of synthesis, characterization and thermo physical properties of Al_2O_3-SiO_2-TiO_2/H_2O based tri-hybrid nanofluid. *Digest Journal of Nanomaterials & Biostructures (DJNB)*. 2021; 16(3): 939-949.
[38] Sohail M, Naz R, Shah Z, Kumam P, Thounthong P. Exploration of temperature dependent thermophysical characteristics of yield exhibiting non-Newtonian fluid flow under gyrotactic microorganisms. *AIP Advances*. 2019; 9(12): 125016. Available from: doi:10.1063/1.5118929.
[39] Ahmed N, Adnan KU, Mohyud-Din ST. Hidden phenomena of MHD on 3D squeezed flow of radiative-H_2O suspended by aluminium alloys nanoparticles. *The European Physical Journal Plus*. 2020; 135(11): 1-7. Available from: doi:10.1140/epjp/s13360-020-00870-2.
[40] Sohail M, Naz R, Abdelsalam SI. On the onset of entropy generation for a nanofluid with thermal radiation and gyrotactic microorganisms through 3D flows. *Physica Scripta*. 2020; 95(4): 045206.
[41] Chu YM, Shankaralingappa BM, Gireesha BJ, Alzahrani F, Khan MI, Khan SU. RETRACTED: Combined impact of Cattaneo-Christov double diffusion and radiative heat flux on bio-convective flow of Maxwell liquid configured by a stretched nano-material surface. *Applied Mathematics and Computation*. 2022; 419: 126883. Available from: doi:10.1016/j.amc.2021.126883.
[42] Hayat T, Ahmad S, Khan MI, Alsaedi A. Modeling chemically reactive flow of Sutterby nanofluid by a rotating disk in presence of heat generation/absorption. *Communications in Theoretical Physics*. 2018; 69(5): 569. Available from: doi:10.1088/0253-6102/69/5/569.
[43] Li S, Puneeth V, Saeed AM, Singhal A, Al-Yarimi FA, Khan MI, et al. Analysis of the Thomson and Troian velocity slip for the flow of ternary nanofluid past a stretching sheet. *Scientific Reports*. 2023; 13(1): 2340. Available from: doi:10.1038/s41598-023-29485-0.
[44] Konai S, Maiti H, Mukhopadhyay S. Influences of Stefan blowing on unsteady flow of Casson nanofluid past a stretching surface. *Forces in Mechanics*. 2023; 12: 100227. Available from: doi:10.1016/j.finmec.2023.100227.
[45] Li S, Khan MI, Alruqi AB, Khan SU, Abdullaev SS, Fadhl BM, et al. Entropy optimized flow of Sutterby nanomaterial subject to porous medium: Buongiorno nanofluid model. *Heliyon*. 2023; 9(7): e17784. Available from: doi:10.1016/j.heliyon.2023.e17784.
[46] Ouada M, Kezzar M, Talbi N, Eid MR, Sari MR, Yousef WM, et al. Heat transfer characteristics of moving longitudinal porous fin wetted with ternary (Cu-Al_2O_3-TiO_2) hybrid nanofluid: ADM solution. *The European Physical Journal Plus*. 2023; 138(9): 1-2.
[47] Alghamdi M, Wakif A, Thumma T, Khan U, Baleanu D, Rasool G. Significance of variability in magnetic

field strength and heat source on the radiative-convective motion of sodium alginate-based nanofluid within a Darcy-Brinkman porous structure bounded vertically by an irregular slender surface. *Case Studies in Thermal Engineering*. 2021; 28: 101428.
[48] Khan WA, Pop I. Boundary-layer flow of a nanofluid past a stretching sheet. *International Journal of Heat and Mass Transfer*. 2010; 53(11-12): 2477-2483.